Directed assembly of Ru nanoclusters on Ru(0001)-supported graphene: STM studies and atomistic modeling

Albert K. Engstfeld, Harry E. Hoster,[*] and R. Juergen Behm

Institute of Surface Chemistry and Catalysis, Ulm University, D-89069, Ulm, Germany

Lyle D. Roelofs

Colgate University, Hamilton, New York, 13346, USA

Xiaojie Liu and Cai-Zhuang Wang

Ames Laboratory—USDOE, Iowa State University, Ames, Iowa 50011, USA

Yong Han[†] and James W. Evans

Department of Physics and Astronomy, Institute of Physical Research and Technology,
and Ames Laboratory—USDOE, Iowa State University, Ames, Iowa 50011, USA

Directed assembly of an array of Ru nanoclusters (NCs) is achieved by deposition of Ru at around room temperature on a single layer of graphene supported on Ru(0001). In this system, directed assembly is guided by the periodic moiré structure of the buckled graphene sheet. Behavior is analyzed utilizing both scanning tunneling microscopy and atomistic lattice-gas modeling together with kinetic Monte Carlo simulation. We elucidate the kinetics of NC nucleation and growth, specifically assessing the coverage dependence of the NC density and height distribution. In addition, we provide a detailed characterization of the development of short-range spatial order within the NC array, identifying a tendency for row formation.

I. INTRODUCTION

A single (mono-) layer of graphene (MLG) supported on transition metal substrates generally displays a periodically modulated moiré structure due to lattice mismatch with the substrate.[1,2] Examples of such transition metal substrates include Ir(111),[3–6] Ru(0001),[7–28] and Rh(111).[29] Modulation of supported MLG offers the possibility for directed assembly of metal nanoclusters (NCs) by vapor deposition of the metal onto the graphene sheet. The formation of such NC arrays in turn has application for model catalyst studies where control of not just the size, but ideally also the spatial arrangement of metal NCs is desired. Demonstration of the directed-assembly concept for metal NCs on supported MLG was provided initially for deposition of Ir on MLG/Ir(111),[3] and subsequently for other metals on MLG/Ir(111).[6] Directed assembly has also been achieved for deposition of various metals on MLG on other transition metal supports. The latter include studies of the deposition of Pt,[22–25] Ru,[26] Pd,[25] and Rh[25] on MLG/Ru(0001), and of the deposition of Ni on MLG/Rh(111).[29]

Our interest here is in the formation of metal NCs on MLG/Ru(0001). Analysis of this class of processes benefits from previous development of structure models for MLG/Ru(0001). Such models, which are based on input from both experiment[7–16] and density functional theory (DFT) analysis,[8,15,17] have provided a detailed characterization of the graphene moiré structure. The experimentally determined area of the moiré cell is $A_M \sim 7.794$ nm².[7] A commonly employed structure model compatible with this A_M value and which we adopt for our atomistic simulations corresponds to a (12×12)C/(11×11)Ru moiré cell.[7,8,10,15,24,25] The area of the Ru(0001) surface unit cell is given by $A_{Ru} = 0.0634$ nm²

($a_{Ru} = 0.2706$, $b_{Ru} = 0.428$ nm). Thus, the area of the moiré cell in units of A_{Ru} satisfies $A^*_M = A_M/A_{Ru} = 122.9$, which is in reasonable agreement with the above structure model value of $A^*_M = 121$. Note that there are also other reasonable choices for a MLG/Ru(0001) structure model.[9,10,16,17]

The moiré cell for MLG/Ru(0001) is a parallelogram composed of an adjacent pair of equal-sized upright and inverted equilateral triangles with a side length of $L_M \approx 2.98$ nm.[8,15,25,26] Three distinct regions in this moiré cell are characterized as follows: atop regions (the vertices of triangles) where C-atom rings surround Ru surface atoms, and hcp and fcc regions (the centers of inverted and upright triangles, respectively, as shown in a schematic provided later in the text) where C-atom rings surround the hcp and fcc hollow sites on Ru(0001). The atop locations are higher by ~0.15 nm than the hcp and fcc regions.[17]

A key feature for directed assembly of NCs for a variety of metals including Ru,[26] Pt,[22–25] and Rh[25] on MLG/Ru(0001) is that the fcc regions act as traps directing the assembly of metal nanoclusters at these locations. This feature is of particular relevance in the current study. For contrast, we note that Co NCs nucleate in both fcc and hcp regions,[27] and Au forms large 2D islands extending over multiple moiré cells[25,28] on MLG/Ru(0001).

The specific focus of this paper is on a detailed analysis of the directed nucleation and growth of Ru NCs during Ru deposition at 309 K on MLG/Ru(0001). Related analysis of the evolution on NC densities is limited in the previous literature,[3,23,25] and no appropriate atomistic-level modeling and simulation has been performed. Analysis of NC diameter and height distributions is more common.[3,22,25,26,29] One might anticipate that the most insight into the underlying energetics
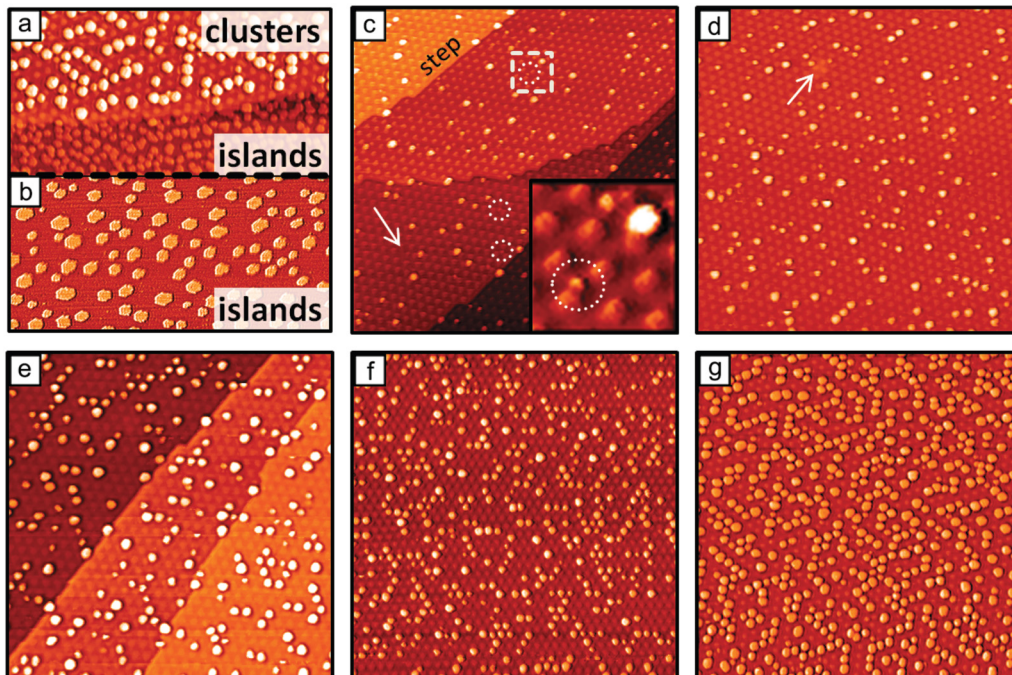
FIG. 1. (Color online) (a) Interface between graphene and the bare Ru substrate. Cluster formation on the graphene (top) and Ru island formation on the substrate (bottom), $\theta = 0.15$ ML, FF $= 45.5\%$; 100×50 nm^2. (b) Hexagonally shaped Ru islands, formed on the bare Ru substrate after annealing for 1 min at 700 K; 100×50 nm^2. Sequence of STM images of Ru clusters grown on MLG/Ru(0001): (c) $\theta = 0.005$ ML, FF $= 13.5\%$, 100×100 nm^2; the dotted circles indicate some small single-layer clusters highlighted in the inset; (d) $\theta = 0.01$ ML, FF $= 17.5\%$, 100×100 nm^2; (e) $\theta = 0.03$, FF $= 26.1\%$, 80×80 nm^2; (f) $\theta = 0.05$ ML, FF $= 34.5\%$, 100×100 nm^2; (g) $\theta = 0.15$ ML, FF $= 47.6\%$, 100×100 nm^2.

should come from analysis of the regime where only a fraction of moiré cells are occupied, even after deposition of a significant coverage of Ru. In this regime, Ru atoms are not simply trapped within the moiré cell where they were deposited. Rather, there exists significant transport between moiré cells, which is a key factor in determining the number, size, and spatial arrangement of NCs. It is appropriate to note that the classic study of Ir NC on MLG/Ir(111)[3] corresponded to a regime where intercell transport was not significant on the timescale of deposition.

In Sec. II, we describe the details of our scanning tunneling microscopy (STM) experiments and present key STM images. Quantitative analysis of experimental results is presented in Sec. III. We not only provide a systematic analysis of the coverage dependence of the mean NC density and NC height distribution, but also quantify the spatial arrangement and ordering of NCs. In Sec. IV, we develop our atomistic lattice-gas model for NC formation, which accounts for the periodic modulation of the supported graphene sheet. This model has broader applicability to metal NC formation on MLG/Ru(0001), but here it is applied only for the Ru/MLG/Ru(0001) system. Results for model behavior from kinetic Monte Carlo (KMC) simulation are presented in Sec. V, and a detailed comparison is made with the experiment. Conclusions are provided in Sec. VI.

II. EXPERIMENTAL DETAILS AND STM IMAGES

The experiments were performed in an ultra-high vacuum (UHV) system with a base pressure of 1×10^{-10} mbar. Clean Ru(0001) surfaces were obtained by cycles of Ar sputtering (0.5 keV Ar$^+$, 4 μA cm^{-2}, $t = 15$ min) and subsequent flashing to 1600 K. In order to obtain a defect-free graphene overlayer, it is essential to remove any remaining carbon impurities from the Ru sample by cycles of oxygen adsorption followed by annealing at 1500 K. For this work, we grow only a partial graphene layer by exposing the Ru(0001) to an ethylene pressure of 5×10^{-9} mbar at 1000 K for 15 min. The temperatures were measured with a pyrometer type IMPAC IGA140 (300–2000 °C). Scanning tunneling microscopy images were acquired in the constant current mode, with typical tunnel currents/voltages of 40–100 pA/1–2 V (applied at the sample).

Ru is deposited onto the partially graphene-covered Ru(0001) surface with an electron beam evaporator (Omicron, EMF3). Ru nanoclusters form on the graphene-covered parts of the surface [Fig. 1(a), top part], as well as on the uncovered parts of the surface [Fig. 1(a), bottom part]. From the graphene-free areas of the Ru(0001) surface, we determine the coverage (θ) of the evaporated Ru, with θ specified in monolayers (ML) with respect to the Ru(0001) surface. However, for deposition around 300 K, the Ru islands are very small [Fig. 1(a), bottom part]. Thus, due to tip convolution, the coverage is always overestimated in STM measurements from these small structures. Therefore, before the coverage measurement, the surface is annealed at 670 K after cluster formation for 1 min to allow for larger hexagonally shaped island formation, as shown in Fig. 1(b). The temperature during evaporation was measured with a type K thermocouple pushed against the Ru crystal.

As noted in Sec. I, graphene growth on Ru(0001) has been studied previously.[7–21] The graphene layer starts growing at the lower Ru step edge and forms mostly defect-free monolayer sheets extending over several terraces.[7,13] The arrows in Figs. 1(c) and 1(d) show defect sites, which consist of dislocations within the graphene layer[7,21] or impurities below the graphene sheet. From images for higher Ru coverages, it is evident that these defect sites are preferred nucleation sites for the Ru NCs. However, for the following statistical analysis of NC nucleation, their effect is negligible since their density corresponds to only about one in 1000 moiré cells (or one in ~100 000 of all the possible adsorption sites). As also noted in Sec. I and illustrated in a figure below, for deposition around 300 K, Ru nanoclusters are only formed in the fcc region of a moiré unit cell.[26] No preference for nucleation at or near step edges of the underlying Ru(0001) surface could be observed [compare Figs. 1(c) and 1(d)].

Results are reported here only for deposition of Ru at 309 K. Figures 1(c)–1(g) show a sequence of STM images of Ru NC arrays corresponding to Ru coverages of 0.005, 0.01, 0.03, 0.05, and 0.15 ML, respectively. Fluxes were in the range of ~0.01 to ~0.1 ML/min, but we note that additional experiments indicate a weak dependence on flux.

At low θ, only a few clusters well separated from each other are found on the surface. Some small one-layer-high NCs are only weakly resolved with STM within a moiré unit cell. Examples of these are marked with dotted circles in Fig. 1(c), and one example is enlarged in the inset. Other larger one-layer-high NCs are clearly visible already at low θ. Increasing θ leads to an increase in the number of NCs on the moiré template, as well as an increase in their size. Inspection of Fig. 1(e) suggests that some of these larger NCs seem to form lines consisting of two to four clusters, a feature seen more clearly for higher θ in Figs. 1(f) and 1(g). See Sec. III for further analysis.

Finally, we note that under our experimental conditions, at most, one Ru NC occupies each graphene moiré cell (and the NC nucleate only in the fcc region). Thus, it is convenient to describe the NC density in terms of the fraction of occupied moiré sites. This so-called filling factor (FF) notation[23] was used in previous studies.[3,6,23] Sometimes FF is quoted as a percentage of occupied cells (rather than as a fraction), so the maximum FF of 100% corresponds to a cluster density of $1/A_M = 0.128$ nm^{-2}.

III. ANALYSIS OF EXPERIMENTAL RESULTS

A. NC filling fraction and height distribution

In Fig. 2, we show the evolution of the filling factor FF with increasing coverage θ for Ru deposition at 309 K from the coverages depicted in Figs. 1(a)–1(g). The absolute error in the FF is approximately 3% as determined by the standard deviation of FF values between 3–6 STM images (with an average of ~1000 moiré cells per image). Small errors or uncertainties due to a variation of the substrate temperature (± 3 K) during the evaporation, as well as due to any flux instability of the evaporator, are not represented in this error assessment. Figure 2 also shows the dependence on θ of the mean size s_{av} of the NCs (measured in atoms). Data comes
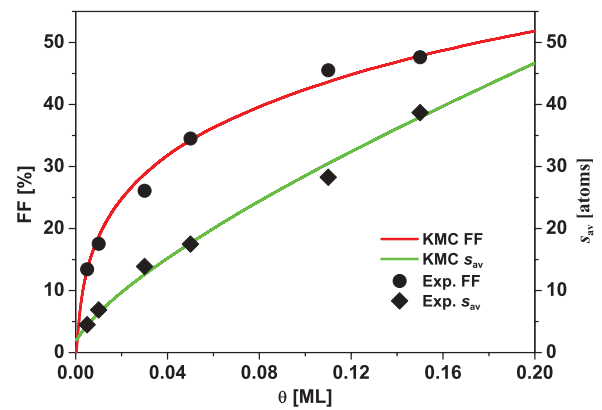

FIG. 2. (Color online) Coverage dependence of filling factor, FF (in %), and mean NC size, s_{av} (in atoms), for Ru deposition at 309 K with fluxes ranging from ~0.01 to 0.1 ML/min. Experimental results are denoted by symbols, and KMC simulations (described in Secs. IV and V) by smooth curves. Simulation parameters are: $E_d = 0.62$ eV, $\delta = 0.28$ eV, $\Delta = 0.20$ eV, $\delta^* = 0.15$ eV, $F = 0.10$ ML/min.

from six separate deposition experiments for the coverages shown, as described in Sec. II.

As noted above, the filling factor FF = FF(θ) is equivalent to a conventional NC density $N = N(\theta)$. For example, one has that $N(\theta) = \text{FF}(\theta)/(100A^*_M)$ when measuring FF as a % and island density as the number of NC per adsorption site on the underlying Ru(0001) support. Note that island density $N(\theta)$ and mean size $s_{av} = s_{av}(\theta)$ measured in atoms are not independent quantities. Rather, they are related by $s_{av}(\theta) = (\theta - \theta_1)/N(\theta)$, where θ is the total coverage and θ_1 is the coverage of isolated diffusing Ru adatoms which are not yet incorporated into NCs (both coverages measured in ML as described above). Since typically $\theta_1 \ll \theta$ for high adatom diffusivity (except for very low θ), one obtains the simple relation $s_{av}(\theta) \approx 12\,100\theta/\text{FF}(\theta)$ using the model value for A^*_M and FF as a %. However, we still show both FF and s_{av} vs θ in Fig. 2, as the possibly simple θ dependence of one quantity could elucidate the less simple variation of the other. For example, Fig. 2 reveals a quasilinear variation of the average NC size $s_{av}(\theta) \approx 8 + 195\theta$ for $0.04 \leqslant \theta \leqslant 0.2$. This implies that FF has the nonlinear form FF(θ) $\approx 12\,100\theta/(8 + 195\theta)$ over this θ range. We emphasize, however, that for lower coverages, $\theta \to 0+$ where $\theta_1 \sim \theta$, one must have that FF(θ) $\to 0$ and $s_{av}(\theta) \to 2$ (as the smallest possible NCs are dimers).

We now comment on general expectations for the θ dependence of FF for metal NCs on MLG supported on transition metal substrates. The general theory of nucleation of NCs via deposition on surfaces[30,31] suggests a short initial transient regime, where the adatom density and thus the NC nucleation rate and FF grow strongly. This is followed by a steady-state regime with a rough balance between the gain of adatoms due to deposition and loss predominantly due to aggregation. Early in the steady-state regime, strong nucleation of NCs persists, and FF continues to grow. Later, a higher NC density can greatly reduce the adatom density. This in turn can effectively terminate nucleation resulting in a postnucleation growth regime with roughly constant FF and a simple proportionality $s_{av}(\theta) \propto \theta$. One simple scenario for
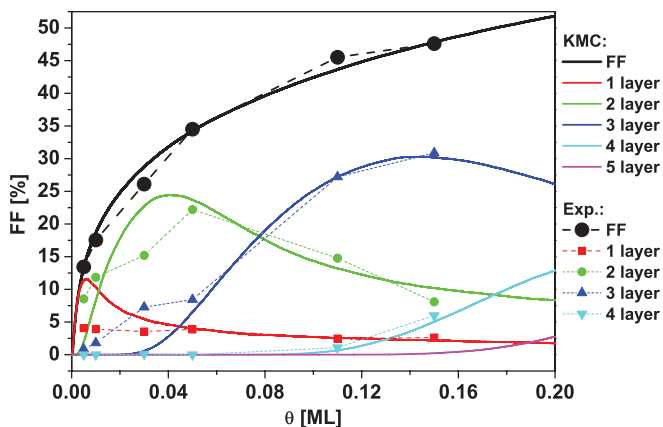
FIG. 3. (Color online) Coverage-dependence NC height distribution described by the filling factors FF($h = 1, 2, \ldots$) of NCs for various specific heights h (measured in layers). Experimental results are denoted by symbols, and simulations (described later) by smooth curves.

metal NCs on MLG/Ru(0001) is that the growth regime could reflect the saturation of the FF at 100%.

From the (noisy) data in Fig. 2 for Ru NC on MLG/Ru(0001), it is tempting to identify a crossover coverage $\theta^* \sim 0.1$ ML for the onset of the growth regime. However, our modeling described below does not find a clear crossover. By way of contrast, STM studies for Ir NC on MGL/Ir(111) reveal that $\theta^* \approx 0.05$ ML at 350 K[3] corresponding to saturation of FF $\approx 100\%$. As an aside, the plot in Ref. 3 of FF in % and S_{av} in atoms for Ir/MLG/Ir(111) uses a common scale, just as in Fig. 2, allowing convenient comparison of behavior in these systems. For Rh NC on MGL/Ru(0001), STM studies reveal $\theta^* \approx 0.8$ ML at 300 K[25] where FF $\approx 24\%$.

Figure 3 presents results for the dependence of the Ru NC height distribution on the coverage θ of Ru deposited on MLG/Ru(0001) at 309 K (from the same experiments used above in the analysis of FF). Specifically, we consider the filling factor FF(h) measured as a percentage (%) of moiré cells populated with NC of a specific height h measured in atomic layers. Thus, one has that FF = FF($h = 1$) + FF($h = 2$) + FF($h = 3$) + $\cdots$ The qualitative evolution is as expected with $h = 1$ NCs first dominating, then $h = 2$ NCs, then the populations of taller NCs dominating. One might anticipate that a stable two-layer NC requires at least 7 Ru atoms (i.e. two bonded nearest neighbor atoms in the second layer requiring a supporting base of 5 Ru atoms in the first layer). Our simulation analysis indicates that observed behavior is consistent with this threshold size for two-layer NCs. In Sec. V, we also deduce threshold sizes for three-layer and higher-layer NCs.

B. Analysis of short-range order in the NC array

Next, we provide a detailed characterization of the arrangement of NCs on the Ru(0001)-supported graphene layer. We assess the populations or densities of various local motifs of NCs, such as nearest neighbor (NN) pairs or dimers and various configurations of trimers. We obtain the dimer density D from the total number of NN dimers divided by the number of moiré cells and divided by the number of distinct orientations (three for dimers). Thus, D corresponds to the probability
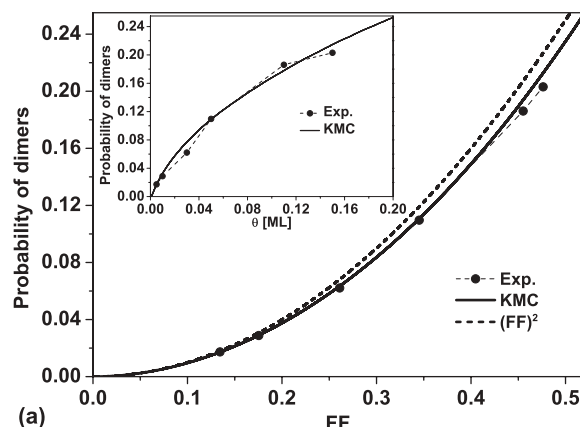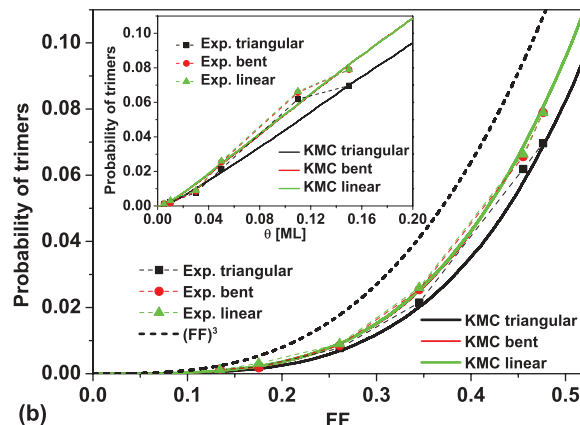
FIG. 4. (Color online) Coverage dependence of the probability of: (a) NC dimers; and (b) linear, bent, and triangular NC trimers in the Ru NC array. Experimental results are denoted by symbols, and simulations (described later) by smooth curves.

that a pair of NN moiré cells will be both populated by NCs. Consequently, D would equal $(FF)^2$ for a random distribution of NCs with FF measured as a fraction of filled cells. In addition, we consider the densities of linear trimers (LT), bent or elbow trimers (BT), and triangular trimers (TT), also obtained as the total number of such species divided by the number of moiré cells and also divided by the number of distinct orientations (three for LTs, six for BTs, two for TTs). Thus, these quantities correspond to the probability that a selected triple of moiré cells with the appropriate configuration are all occupied by NCs. Thus, LT, BT, and TT would all correspond to $(FF)^3$ for a random distribution of NCs.

Results are shown in Fig. 4 for the probabilities for all these motifs vs FF measured as a fraction (and also as a function of coverage θ in the insets). To a first approximation, the dependence on FF might be characterized by

$$D \sim (FF)^2 \text{ and } LT, BT, TT \sim (FF)^3. \tag{1}$$

This behavior corresponds to a random distribution of NCs, although there are clear deviations, as discussed in detail below. However, first, here we wish to draw attention to the coverage dependence of FF illustrated in the insets and in particular to the near proportionality

$$LT, BT, TT \propto \theta. \tag{2}$$

TABLE I. Comparison of experimental trimer probabilities (TT = triangular, BT = bent/elbow, LT = linear) with predictions from the Kirkwood approximation (which incorporates the experimental dimer probabilities and FF values).

Coverage (ML)	FF (%)	D (expt)	TT (expt)	TT (Kirkwood)	BT (expt)	LT (expt)	BT, LT (Kirkwood)
0.01	17.5	0.029	0.0021	0.0044	0.0018	0.0031	0.0047
0.03	26.1	0.062	0.0078	0.0135	0.0085	0.0090	0.0148
0.05	34.5	0.110	0.0215	0.0320	0.0254	0.0260	0.0348
0.15	47.6	0.203	0.0697	0.0775	0.0789	0.0789	0.0866

To interpret this feature, consider the nucleation and growth of NCs with a critical size i (above which clusters are stable). Standard nucleation theory implies that FF $\sim \theta^{i/(i+2)}$ in the predominant quasisteady-state regime, where there is a rough balance between gain of diffusing adatoms on the surface due to deposition and loss due to aggregation.[30,31] It follows that LT, BT, or TT $\sim$ (FF)$^3 \sim \theta^{3i/(i+2)}$. Consequently, the observed linear dependence corresponds to a critical size $i = 1$, as might be expected for nucleation at ~300 K given the strength of Ru-Ru adatom interactions. The conclusion that FF $\sim (\theta)^{1/3}$ also explains the sublinear variation of D with θ. It should be noted that usually critical size is assessed by considering flux dependence of the NC density or the shape of the size distribution.[31] However, here, we have another possibility, e.g. through analysis of trimer probabilities.

The feature that the dimer and trimer probabilities in Fig. 4 are below those expected for a random distribution of NCs reflects anticlustering of NCs. Anticlustering is also a general feature of NC nucleation on unstructured surfaces,[30,31] which should extend to nucleation on structured substrates in the regime of interest here. Nanoclusters act as sinks for diffusing adatoms. Consequently, the adatom density is reduced in the vicinity of existing NCs and more specifically in this case in the moiré cells which neighbor NCs. This, in turn, reduces the rate of NC nucleation in such neighboring moiré cells and thus reduces the population of NCs nearby other NCs. One might regard this feature as corresponding to an effective repulsion between NCs. More detailed consideration indicates that the density of diffusing adatoms should be more strongly depleted in a moiré cell adjacent two NCs, and thus the formation of a triangular trimer from a dimer should be more strongly inhibited than the formation of linear or bent trimers. Results in Fig. 4 are entirely consistent with this prediction. A refined analysis would suggest a slight preference for linear over bent trimers, but this appears to be a negligible effect.

One can quantify this behavior in terms of conditional filling fraction FF$_c$ where this and other quantities are measured below as a fraction (rather than as a %). To define this quantity, consider a neighboring pair of moiré cells. Suppose that one of these is specified to be populated by an NC, then FF$_c$ gives the conditional probability that its neighbor is populated by an NC. It follows that

$$\text{FF}_c \equiv D/\text{FF} \quad (\text{so that } D = \text{FF} \cdot \text{FF}_c). \qquad (3)$$

Note that FF$_c <$ FF (FF$_c >$ FF) corresponds to anticlustering (clustering). A Kirkwood-type superposition approximation[32] or pair approximation[33] adapted for the statistics of trimers

predicts that

$$\text{LT} \approx \text{BT} \approx (D)^2/\text{FF} = \text{FF} \cdot (\text{FF}_c)^2 \quad \text{but that}$$
$$\text{TT} \approx (D)^3/(\text{FF})^3 = (\text{FF}_c)^3. \qquad (4)$$

Consequently, TT is expected to be smaller within this approximation than LT or BT (which are identical). These trends are entirely consistent with experimental observations. However, the Kirkwood approximation cannot capture with quantitative precision the spatial correlations in the NC distribution (see Table I). We shall see that exactly the same type of discrepancy with the Kirkwood estimates arises in our simulation results, a feature which supports the effectiveness of our modeling.

Another feature apparent from the STM images is a propensity for the formation of straight rows of neighboring NCs, at least for higher values of FF. Although perhaps counterintuitive, this behavior is actually consistent with the above observations on anticlustering of NCs. Insight into this behavior follows from two observations:

(i) For a scenario where most NCs are incorporated into long nonadjacent linear rows of NCs, one obtains FF$_c(r = 1) = 1/3$ independent of FF. Thus, when FF $> 1/3$, formation of nonadjacent rows corresponds to anticlustering and should be expected given the above discussion. For FF $< 1/3$, there should be no propensity for row formation.

(ii) For higher FFs where at least short segments of isolated rows have already formed, consider the nucleation of nearby NCs. Cells along the edge of the row have two neighboring NCs and thus a lower adatom density than cells at the end with one neighboring NC. As a result, nucleation is inhibited along the sides relative to the end.

Both the above observations rely on the feature that the fcc moiré half cells form a triangular grid with coordination number 6. Thus, the propensity for row formation would be absent (or at least greatly reduced) for a square grid.

Extending the considerations of item (ii) above, there are three cells at the end of a row of NCs with a single neighboring NC, one aligned with the NC row, and the other two at an angle of 60° all with a single neighboring NC. The adatom density in these cells should be similar, but that in the aligned cell should be slightly higher. This in turn should enhance the growth of linear rather than bent rows, recalling that nucleation is very sensitive to adatom density.[30,31]

We can also extend the above consideration of dimer statistics to more general features of short-range order (SRO) associated with two-point spatial correlations in the array of NCs. Specifically, extending the definition of FF$_c$, we let FF$_c(\mathbf{r})$ denote the conditional probability that a moiré cell is occupied by a NC, given that it is separated by $\mathbf{r}$ from another cell, which is specified to be occupied. One determines
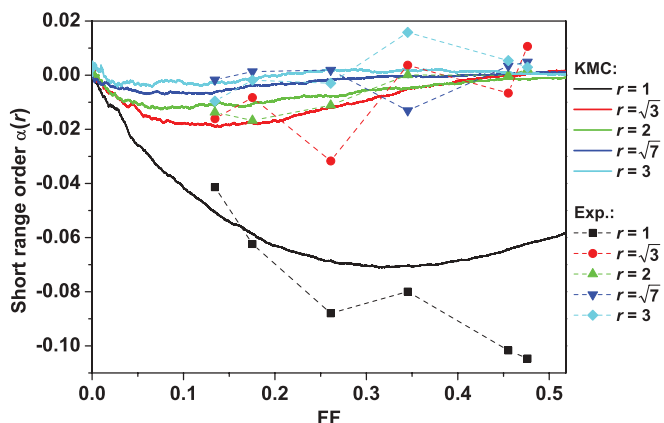
FIG. 5. (Color online) Dependence on FF of two-point SRO parameters $\alpha(r)$ in the Ru NC array corresponding to $r = 1, \sqrt{3}, 2, \sqrt{7}$, and 3 (in units of the moiré cell lattice constant). Experimental results are denoted by symbols, and simulations (described later) by smooth curves.

distinct values for separations $r = |\mathbf{r}| = 1, \sqrt{3}, 2, \sqrt{7}, 3, \ldots$ measured in units of the nearest neighbor (NN) cell separation. Then, the above conditional filling fraction is recovered from $FF_c = FF_c(r = 1)$. Traditional SRO parameter(s) are defined as

$$\alpha(r) = \{FF_c(r)/FF\} - 1$$
$$> 0 \; (< 0) \text{ for clustering (anticlustering).} \quad (5)$$

The experimental results are presented in Fig. 5 showing the variation of $\alpha(r)$ with FF. The data correspond to anticlustering with $\alpha(r) < 0$, although this feature quickly weakens (i.e. spatial correlations become very small) for increasing $r > 1$.

Finally, we offer some brief comments on the dependence of SRO on coverage or FF. There is little analysis of the coverage dependence of spatial correlations in classic surface nucleation theory,[30,31] and in any case this would be of limited use for the current study. It is clear that $\alpha(r) \to 0$ (vanishing correlations), as FF $\to 0$ (low NC population), and as FF $\to 1$ (maximal population). Maximum amplitudes occur at intermediate FF. Substantial noise in the experimental data precludes a clear picture, so we defer further discussion until the following section on modeling.

IV. ATOMISTIC MODELING: DIRECTED ASSEMBLY OF NCs

Our atomistic lattice-gas modeling for Ru NC formation on MLG/Ru(0001) assigns the adsorption sites k for isolated diffusing Ru adatoms as a triangular lattice (coordination number 6) corresponding to hollow sites in the center of the C rings of the graphene sheet. Deposition of Ru occurs randomly on these sites at an experimentally determined rate, and diffusion of isolated Ru adatoms occurs via hopping to one of the six neighboring sites. Consistent with the $(12 \times 12)C/(11 \times 11)Ru$ model for MLG/Ru(0001), the key energetic parameters characterizing Ru adsorption vary with a 12×12 periodicity, reflecting the moiré structure of the modulated graphene layer. Given our focus on low coverages well below the coalescence regime, we adopt a convenient

and efficient point island model which can accurately describe key aspects of nucleation and growth in this regime.[34–36] This model tracks the size of each island, but does not describe island structure, rather just treating each island as occupying a single site. In addition, we treat both nucleation and aggregation as irreversible (two Ru atoms form a stable nucleus for an NC corresponding to a critical size of unity) given the experimental evidence presented in Sec. III for critical size $i = 1$. Also, all NCs of two or more Ru atoms are treated as immobile (but see discussion below of postdeposition effects).

A. Benchmark model: Thermodynamically directed assembly of NCs

Now we describe in more detail our benchmark model in which directed assembly of Ru NCs in the fcc regions is thermodynamically driven. We assume that the adsorption energy $E_{ads}(k)$ for Ru adatoms at adsorption sites k varies periodically across the moiré cell illustrated in Fig. 6(a). The strongest binding corresponds to a global minimum $E_{ads}(fcc)$ of E_{ads} occurring at the center of the fcc half-cell. Weaker binding at the center of the hcp half-cell generally corresponds to a local minimum in E_{ads} which is above the fcc value by Δ. Binding can be even weaker along the linear fcc-hcp boundary with a saddle point in E_{ads} occurring at the center of this boundary above the fcc value by $\delta \geqslant \Delta$. The weakest binding, corresponding to a global maximum in E_{ads} above the fcc value by $\delta + \delta^*$, generally occurs at the atop sites of the moiré cell (when $\delta^* > 0$).
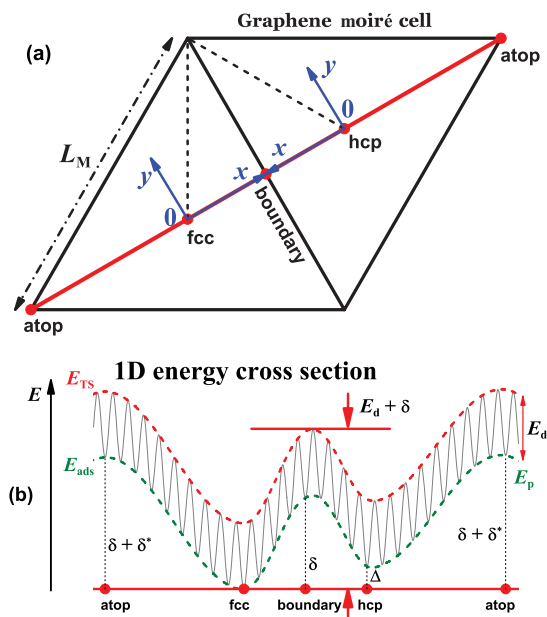

FIG. 6. (Color online) (a) Schematic of the graphene moiré unit cell; (b) 1D schematic of the binding energy variation for an Ru adatom across the moiré cell for our benchmark model showing the coarse-scale variation described by E_p (dashed curve) and fine-scale variation (oscillatory thin curve). The 2D variation of E_p in the small triangle corresponding to 1/6 of the fcc half-moiré cell with x and y axes shown is described by $E_p = \delta \sin^2[\pi\sqrt{3}x/L_M] + \delta^* \sin^2[\pi y/L_M]$. Behavior in 1/6 of the hcp half-moiré cell is described by $E_p = \Delta + (\delta - \Delta) \sin^2[\pi\sqrt{3}x/L_M] + \delta^* \sin^2[\pi y/L_M]$.
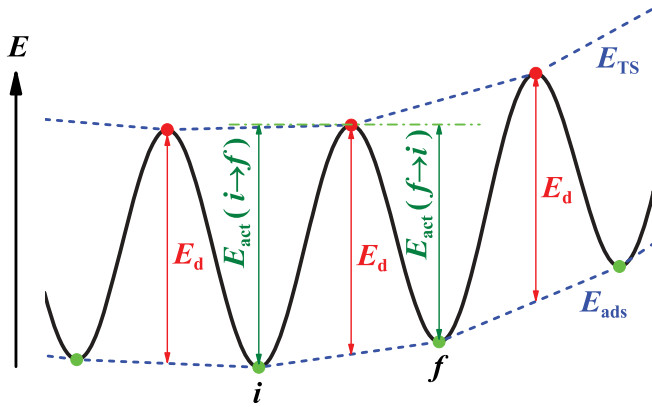
FIG. 7. (Color online) Fine-scale variation of the potential energy surface in the benchmark model for an Ru adatom hopping between neighboring adsorption sites i and f on MLG/Ru(0001).

The above behavior is captured by expressing the adsorption energy in the form $E_{ads}(k) = E_{ads}(fcc) + E_p(k)$, where again k labels the adsorption sites and the energy function $E_p(k) \geqslant 0$ describes the coarse-scale periodic variation of E_{ads} across the moiré cell.[37] This coarse-scale energy variation is indicated in Fig. 6(b) by the dashed lines. The three key energy parameters Δ, δ, and δ^* are also indicated. The fine-scale variation of the adsorption energy as the lateral adatom position varies continuously between neighboring adsorption sites is also indicated in Fig. 6(b) by the oscillatory thin solid curve.

The energetic input to the model is exclusively through specification of the activation barrier $E_{act}(i \rightarrow f)$ to hop from an initial site i to an adjacent final site f. In our benchmark model, we choose the form

$$E_{act}(i \rightarrow f) = E_d + [E_{ads}(f) - E_{ads}(i)]/2$$
$$= E_d + [E_p(f) - E_p(i)]/2. \quad (6)$$

The parameter E_d corresponds to a constant average local diffusion barrier in the sense that it gives the average of the barriers for forward and reverse hops between an adjacent pair of sites. Actual barriers for hopping vary just slightly from E_d given the slow variation of E_p. Roughly speaking, one can think of Eq. (6) as corresponding to a fixed energy difference between the adsorption site energies E_{ads} and the transition state energies E_{TS}. One can also regard E_d as the barrier which would apply in flat regions of the modulated graphene sheet, and also plausibly E_d reflects the barrier for Ru diffusion on an unsupported graphene sheet.

This specification in Eq. (6) of E_{act} is consistent with detailed balance given our prescribed variation of the adsorption energy. This specification may be translated into the detailed picture of fine-scale variation of the adsorption energy shown in Fig. 7. The hopping rates are selected to have the Arrhenius form $h(i \rightarrow f) = \nu \exp[-E_{act}(i \rightarrow f)/(k_B T)]$ with a common prefactor $\nu = 10^{13}$/s.

A consequence of the choice in Eq. (6) is that the quasiequilibrium density of adatoms (if NC nucleation is suppressed) would be maximized in the fcc regions as these have the strongest binding. Since the local NC nucleation rate scales as the square of the local adatom density (for $i = 1$), this rate is enhanced in those regions of higher density. This explains the thermodynamically directed assembly of NCs. We caution that it will be necessary to choose Δ sufficiently large to avoid significant formation of NCs in the hcp region.

Finally, we discuss the ramifications of the choice in Eq. (6) for long-range diffusive transport. For $\delta > \Delta$, the effective barrier to cross from the fcc to the hcp region is $E_{eff} = E_d + \delta$ with a saddle point in E_{act} at the midpoint of the linear fcc-hcp boundary [see Fig. 6(b)]. The effective additional barrier in the reverse direction is $E'_{eff} = E_d + \delta - \Delta$. The model describes biased diffusion on the surface with a preference (i.e. higher rates) for hopping towards the center of the fcc and hcp regions which are global or local minima of E_{ads}. We expect the FF to be strongly dependent on E_d and δ, but less so on δ^*.

B. Alternative energy variations for directed assembly

Generic continuum formalisms of directed assembly have considered behavior for four distinct forms of the coarse-scale variation of two key energies: the adsorption energy E_{ads} and the energy at the transition state E_{TS} for hopping between adjacent sites:[38] (i) in-phase periodic variation of both E_{ads} and E_{TS} as in our benchmark model of Sec. IV A; (ii) periodic variation of E_{ads} and constant E_{TS}; (iii) out-of-phase periodic variation of E_{ads} and E_{TS}; (iv) constant E_{ads} and periodic variation of E_{TS}. In the continuum description, diffusion has the local barrier $E_{act} = E_{TS} - E_{ads}$ (which is constant for case (i) as in the model in Sec. IV A), but there is also a drift term in cases with a gradient in E_{ads}. Our following discussion of the behavior of these various models extends the characterization in Sec. IV A to note that the local NC nucleation rate is given by the local hop rate or diffusion rate times the square of the local adatom density.

All of cases (i)–(iii) incorporate a thermodynamic driving force for directed assembly with NCs at the minima of E_{ads}, since at this location the quasi-equilibrium density of adatoms is maximized. In case (ii), this tendency for directed assembly is reduced by slower diffusion in the fcc regions, given the above observation that the nucleation rate is reduced for slower diffusion. In case (iii), this reduction is even stronger and can completely eliminate directed assembly or redirect assembly to the regions with the highest diffusion barrier.

To elucidate the effect of variable diffusivity, it is most convenient to consider case (iv), where the quasi-equilibrium adatom density is constant across the surface. Thus, directed assembly is purely kinetically driven and occurs in regions of highest diffusion rate (or lowest barrier). This is in some sense the opposite of case (i). Of interest is the strength of directed assembly in case (iv) and whether the experimentally observed behavior can be achieved for a reasonable choice of energetic parameters. To craft such a model (iv), one can again utilize a coarse-scale periodic function E_p with a minimum in the fcc region as shown in Fig. 6(b). Now the model input energetics involves a barrier to hop from site i to neighboring site f with the distinct form $E_{act}(i \rightarrow f) = E_{act}(f \rightarrow i) = E_{d0} + [E_p(f) + E_p(i)]/2$, where E_{d0} now corresponds to the minimum diffusion barrier occurring just in the fcc region. The Arrhenius form of the hop rate is consistent with detailed balance for constant E_{ads}. We will briefly describe results for this alternative model in Sec. V C.

Finally, one should ask which case best describes the actual behavior for Ru/MLG/Ru(0001). The general expectation, supported by limited DFT analysis is that E_{ads} varies with strongest binding in the fcc region.[26] While there is no comprehensive analysis for Ru/MLG/Ru(0001), a study of a related system[39] suggests that there is some tendency for in-phase variation of E_{ads} and E_{TS} as in case (i). Thus, we focus on this benchmark model below.

V. KMC SIMULATION RESULTS

Analysis of the above models is achieved by KMC simulation, where one implements random deposition of Ru atoms and hopping of Ru adatoms with probabilities proportional to the physical rates for these processes. Again, nucleation of Ru NCs is irreversible, occurring when two diffusing adatoms meet, and aggregation with Ru NCs is also irreversible. Thus, these processes do not introduce extra rates, noting that in the point-island model,[34] there is no need to describe periphery diffusion. One complication is that an isolated Ru adatom in a half-moiré cell can undergo rapid correlated diffusion within a single half-cell (with high hop rates towards the center in the benchmark model). This can significantly increase the computational expense of the simulation, which can become prohibitive for smaller E_d. Results are presented for our benchmark model incorporating thermodynamically driven assembly unless otherwise stated.

A. KMC results for NC filling factor

Our initial goal is to determine whether experimentally observed values for filling factor (FF) can be obtained with a reasonable choice of energetics in our benchmark atomistic model. One previous DFT study[40] for Ru on freestanding graphene indicated the strongest binding at the hollow site in the center of the C ring, as indicated above. It also indicated weaker binding by 0.72 eV above a C atom, and by 0.75 eV above a C-C bond. This implies a diffusion barrier of $E_d = 0.72$ eV for hopping between hollow sites over C atoms. A subsequent study by this group reported a substantially higher barrier closer to 1 eV.[41] However, simulation results for our model with E_d of 0.70 eV or above produced FF significantly larger than experiment (unless values for other parameters were selected to be very low, which resulted in NC population of the hcp regions). We find that reducing E_d to the range 0.58–0.65 eV yields good agreement for reasonable values of other parameters. This apparent discrepancy prompted our own DFT analysis for Ru adsorption and diffusion on freestanding graphene obtaining a revised value of $E_d = 0.62$ eV consistent with estimates from KMC (see the Appendix).

Simulations were performed varying model parameters and comparing results against experiment. These indicate that it is possible to obtain a reasonable match to the experimentally observed variation of FF vs θ, at the same time essentially exclusively populating the fcc regions with NCs at 309 K.[42] One such choice of parameters using $E_d = 0.62$ eV which matches our DFT result is: $\delta = 0.28$ eV, $\delta^* = 0.15$ eV, and $\Delta = 0.20$ eV. Figure 8 shows simulated NC distribution with these parameters for two values of FF = 24% and 48%. Figure 2 compares behavior for FF vs θ for these parameters
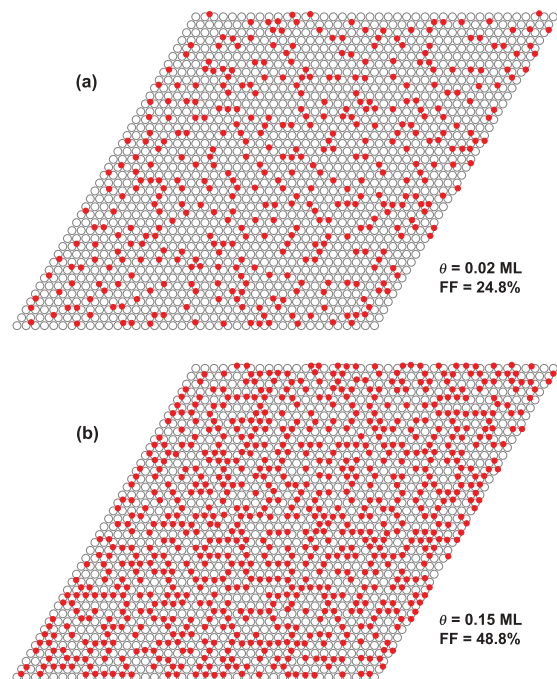

FIG. 8. (Color online) Spatial arrangement and SRO of NCs from KMC simulation of the benchmark model with $E_d = 0.62$ eV, $\delta = 0.28$ eV, $\delta^* = 0.15$ eV, and $\Delta = 0.20$ eV at 309 K.

with experiment. An alternative parameter choice is motivated by the proposal of Sutter *et al.*[26] that the Ru adsorption energy in both hcp and atop regions is weaker than that in fcc regions by a similar amount of ~0.4 eV. This motivates consideration of choices with $\delta = \Delta$ and $\delta^* = 0$, and we find that selecting $E_d = 0.58$ eV and $\delta = \Delta = 0.40$ eV also matches experiment. The plot of FF vs θ for this case is almost identical to the above choice. Other possible choices are discussed in detail below.

From our simulation analysis, in addition to reliable values for FF, we can readily determine uncertainties in estimates of FF (given below in %) for measurements or simulations with a finite (limited) system size. The relevant formulation derives from a fluctuation-correlation relation[31] for the number M of NCs expected in a finite system of $L \times L$ moiré cells:

$$\langle (M - \langle M \rangle)^2 \rangle \sim c(\theta) \, L^2 \quad \text{so}$$
$$\langle (\text{FF} - \langle \text{FF} \rangle)^2 \rangle \sim 10^4 \, c(\theta) L^{-2}. \quad (7)$$

We find that $c(\theta) \approx 0.028, 0.086, 0.045$ for $\theta = 0.01, 0.05, 0.15$ ML, respectively. Thus, the uncertainty in FF estimated from a standard deviation $\sigma_{FF} \approx 100 c^{1/2}/L \sim 0.2\%$ is small for a simulation in a 100×100 cell system. Our results come from averaging N_{trial} such simulations further reducing the uncertainty by a factor of $(N_{trial})^{-1/2}$.

As indicated above, there is not a unique choice of energetic parameters which alone reasonably matches experiment. Thus, some relevant trends observed from extensive simulations upon varying model parameters are reported below:

(i) Varying E_d and δ in opposite directions, roughly preserving $E_{eff} = E_d + \delta$, can maintain the match with, for example, FF $\approx 48.1\%$ at $\theta \approx 0.15$ ML in experiment. In Table II, we give two examples of this behavior, one for fixed $\Delta = 0.2$ eV and $\delta^* = 0.15$ eV, and the other for $\Delta = \delta$

TABLE II. Parameter choices matching FF $\approx$ 48.1% at $\theta \approx 0.15$ ML in experiment by varying E_d and δ in opposite directions. All energies in eV.

$\Delta = 0.20$ $\delta^* = 0.15$			$\Delta = \delta$ $\delta^* = 0$				
E_d	0.60	0.62	0.64	E_d	0.58	0.60	0.62	0.65	0.68
δ	0.34	0.28	0.22	δ	0.40	0.35	0.305	0.23	0.145

and $\delta^* = 0$ (cf. Ref. [26]). However, constraining E_d to around our DFT value limits the choice of the other parameters.

(ii) The sensitivity of FF to δ^* and Δ should be weaker than to δ (allowing one parameter to vary and holding the others fixed). Specifically, FF will increase strongly with δ, as this increases the effective barrier to long-range transport E_{eff}. The same is not true for varying δ^* and Δ. The weakest dependence of FF is with δ^*, as changing δ^* does not affect the potential energy surface along the diffusion path, but presumably does change the effective prefactor. These trends are confirmed in Table III.

We now provide some additional discussion of the more subtle aspects of the model parameter dependence. First, consider the dependence of FF on Δ keeping the other parameters fixed. As Δ increases, this reduces the residence time in hcp regions and thus enhances long-range mass transport. One might think that this would reduce FF. However, the opposite trend occurs (see Table III). Presumably for lower Δ, the hcp regions act as a reservoir for Ru adatoms lowering their density in fcc regions and thus lowering the nucleation rate in those regions which in turn lowers FF. Second, we consider further behavior upon varying E_d and δ in opposite directions while keeping FF fixed. Note that as E_d increases, the effective barrier $E_{eff} = E_d + \delta$ must be made smaller. Why? Increased E_d lowers the nucleation rate which must be compensated for by enhancing long-range transport.

It should be noted, however, that for all of these parameter choices matching the experimental FF, we expect the other basic features of the model behavior discussed below (height distributions, short-range order, size distributions) to be fairly robust.

B. KMC results for NC size and height distributions

Next, we use our atomistic modeling to estimate the evolution of the NC height distribution during deposition. It should be emphasized that our point-island modeling does not explicitly describe the structure of the NCs, but rather only their sizes. Thus, some additional hypothesis is needed to

TABLE III. Sensitivity analysis of FF (in %) to various energetic parameters varying parameters one at a time about $E_d = 0.62$ eV, $\delta = 0.28$ eV, $\delta^* = 0.15$ eV, and $\Delta = 0.20$ eV.

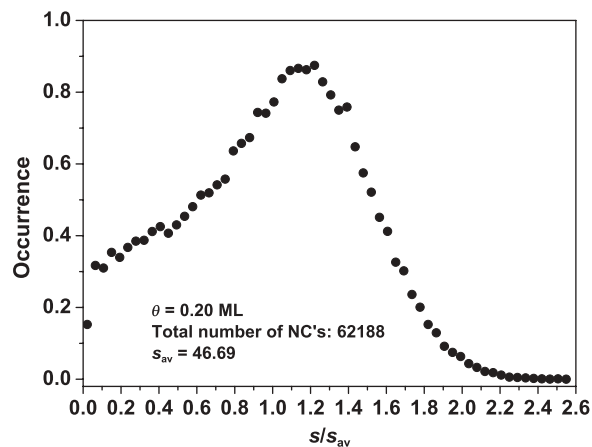| $\delta - 0.28$	FF $- 48.1$	$\Delta - 0.15$	FF $- 48.1$	$\delta^* - 0.20$	FF $- 48.1$
-0.03	-9.2	-0.05	-3.0	-0.05	-2.7
-0.01	-3.2	-0.01	-0.6	-0.01	-0.9
$+0.01$	$+3.5$	$+0.01$	$+0.5$	$+0.01$	$+0.3$
$+0.03$	$+10.0$	$+0.05$	$+4.8$	$+0.05$	$+0.9$

FIG. 9. Scaled NC size distribution where the area under the scaled plot is unity (Ref. [31]). The total number of NCs used to obtain this low-noise data is also indicated.

convert size to structure or height. We will assume that there are reasonably well-resolved threshold sizes $S_{h \to h+1}$ (measured in atoms) for the transition from NC height h to $h + 1$ layers for $h = 1, 2, \ldots$ Thus, the picture is that when an NC reaches a threshold size $S_{h \to h+1}$, it quickly converts to the greater height $h + 1$. Consider the extreme case with a very strong propensity for 3D NC formation, but where a stable NC and requires at least one nearest neighbor pair of Ru atoms in the top-most layer. Accounting for hcp stacking, one has $S_{1 \to 2} = 7$, $S_{2 \to 3} = 17$, $S_{3 \to 4} = 33$, etc.[43] However, the observed behavior does not match this choice.

From our atomistic point-island simulations, we can generate the complete NC size distribution, FF_s (the filling factor for NCs of s atoms), where one has that $FF = \sum_{s \geqslant 2} FF_s$. A scaled version of this distribution is shown in Fig. 9. This distribution has the standard shape expected for irreversible NC formation.[31,34,35] It is significantly broader than the Poisson distribution, which applies if there is no transport between moiré cells,[3] and for which the width of the corresponding scaled distribution decreases with increasing mean NC size. Thus, given a selection of the $S_{h \to h+1}$, we can determine $FF(h = 1) = \sum_{2 \leqslant s < S1 \to 2} FF_s$, $FF(h = 2) = \sum_{S1 \to 2 \leqslant s < S2 \to 3}$ FF_s, etc. and their variation with θ for comparison with experiment. As indicated above, the smallest viable choice of $S_{h \to h+1}$ listed above is not consistent with experiment. However, we find that a choice $S_{h \to h+1} = 7, 26, 60, 80, \ldots$ for $h = 1, 2, 3, 4, \ldots$ does provide a reasonable match (see Fig. 3).

C. KMC results for NC short-range order

One advantage of our atomistic simulation model is that we can characterize not just FF behavior as in Fig. 2, but also the spatial arrangement of NCs from analysis of images like Fig. 8, for comparison with experiment. Specifically, we can analyze the probabilities of dimer and various trimer configurations, as well as general two-point SRO parameters. Simulation results track experimental behavior as shown in Figs. 3 and 4. It is instructive to also compare the probabilities of various trimers measured directly from KMC simulations with the predictions from the Kirkwood approximation consistently

TABLE IV. Comparison of trimer probabilities (TT = triangular, BT = bent/elbow, LT = linear) from KMC with predictions of the Kirkwood approximation (based on dimer probability and FF values from KMC).

Coverage (ML)	FF (%)	D (KMC)	TT (KMC)	TT (Kirkwood)	BT (KMC)	LT (KMC)	BT, LT (Kirkwood)
0.01	18.65	0.0326	0.0019	0.0054	0.00269	0.00284	0.00573
0.03	28.76	0.0769	0.0101	0.0191	0.01285	0.01303	0.02058
0.06	36.26	0.1222	0.0243	0.0383	0.02993	0.03038	0.04121
0.15	47.84	0.2147	0.0700	0.0903	0.08188	0.08192	0.09631

using the dimer probability from simulations. Table IV reveals that the Kirkwood approximation correctly predicts qualitative trends but not quantitative values with exactly the same type of discrepancy as was found in the analysis of the experimental data. This supports the effectiveness of our model in capturing experimental behavior.

Obtaining sufficiently precise results for this analysis is more challenging, as we are interested in intrinsically small quantities like SRO parameters, or in comparing close quantities such as D vs $(FF)^2$ or various trimer probabilities. As a result, it was necessary to average results from multiple simulations ($N_{trial} = 12$) for a 100×100 moiré cell system. To give some insight into these uncertainties, we mention that the standard deviation in trimer probabilities for simulations in a 100×100 cell system varies from $\sigma_T \sim 0.0003$ for $\theta = 0.01$ ML to $\sigma_T \sim 0.001$ for $\theta = 0.05$ ML to $\sigma_T \sim 0.001$–0.002 for $\theta = 0.15$ ML. However, discrimination of very small differences in probabilities for linear and bent trimer configurations requires multiple trials. For the SRO parameters $\alpha(r)$, the standard deviation for simulations in a 100×100 cell system are of the order $\sigma_\alpha \sim 0.002$–0.004. Since these standard deviations vary like $1/L$, the use of smaller STM images for extracting results produces significant uncertainties in experimental estimates. However, our simulation analysis of the SRO behavior uses sufficient trials ($N_{trial} = 12$) to effectively eliminate uncertainties and provide a clear picture of the variation of SRO parameters with FF and of the decrease in the magnitude of these quantities with increasing r (see Fig. 4).

Finally, we briefly comment further on the propensity for formation of NC rows at higher values of FF, which is clear from both experimental and simulation images of NC spatial distributions. Consider the quasisteady-state density for diffusing atoms in the vicinity of the end of an already formed row of NCs (see Fig. 10). Solution of the appropriate steady-state diffusion equation treating the NCs in the row as sinks for diffusing atoms reveals that the adatom density is much lower on the edge fcc moiré half cells (e_j) than at the end bent (b) or straight (s) half cells. (In this analysis, it is necessary to also impose a suitable effective outer boundary condition, or to include an effective loss term, to account for adatom capture by other NCs.) The density at s is slightly higher than at b. Thus, NC nucleation is relatively inhibited at e_j, and enhanced at b and s (slightly more at the latter).

D. Additional KMC results: Propensity for directed assembly

How great a thermodynamic driving force is required to direct assembly of NC almost exclusively to the fcc regions? The benchmark model for thermodynamically directed assembly requires Δ above $\sim$0.1 eV (i.e. adsorption in hcp regions is less favorable by $\sim$0.1 eV or above). For example, with the parameter choice $E_d = 0.62$ eV, $\delta = 0.28$ eV, $\delta^* = 0.15$ eV, which matches experiment for $\Delta = 0.20$ eV with FF = 48.1% at $\theta = 0.15$ ML at 309 K, one finds that the fraction of NC in the hcp region or on the fcc-hcp boundary increases to $\sim$1% upon lowering Δ to 0.15 eV (where FF = 45.1%), and to $\sim$4% upon lowering Δ to 0.10 eV (where FF $\approx$ 43.5%). With the alternative choice $E_d = 0.68$ eV, $\delta^* = 0$, and $\Delta = \delta$, the fraction of hcp or fcc-hcp boundary NC increases from $\sim$1.4% when $\Delta \approx 0.15$ (with FF $\approx$ 48% matching experiment), to $\sim$6% (with FF $\approx$ 40%) when $\Delta = 0.10$ eV, to $\sim$26% (with FF $\approx$ 39%) when $\Delta = 0.05$ eV.

Finally, we briefly present some results from our alternative model for kinetically directed assembly where E_{ads} is constant. We choose the Ru adatom diffusion barrier to smoothly increase from a minimum value of E_{d0} in the center of the fcc half-cell to a value of $E_d + \varepsilon$ at the fcc-hcp boundary and to maintain this higher value throughout the hcp half-cell. Specifically, we choose $E_{act}(i \rightarrow f) = E_{act}(f \rightarrow i) = E_{d0} + [E_p(f) + E_p(i)]/2$, where the parameters in E_p are now set to $\delta = \Delta = \varepsilon$ and $\delta^* = 0$. First, we note that we can recover the experimentally observed FF = 48.1% at $\theta = 0.15$ ML at 309 K for a range of E_{d0} and ε varying these in opposite directions, e.g. $E_{d0} = 0.62, 0.65, 0.66, 0.67, \ldots$ eV and $\varepsilon = 0.26, 0.19, 0.16, 0.12, \ldots$ eV, respectively. However, the fraction of NCs nucleated in hcp or fcc-fcp boundary regions naturally increases ($\sim$0%, 0.4%, 1%, 3%, 30%, respectively) with decreasing ε.
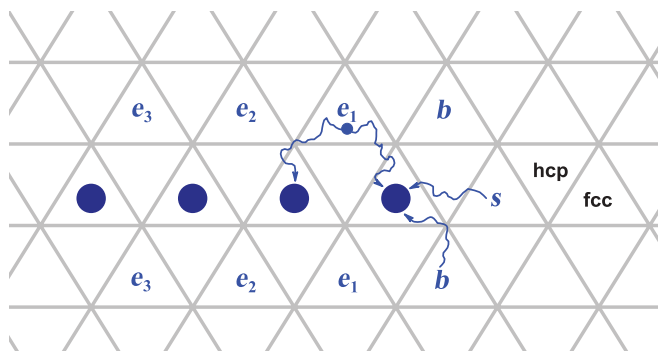

FIG. 10. (Color online) Adatom diffusion and capture near the end of a row of NCs. The figure labels edge (e_j), end bent (b), and straight (s) fcc half-moiré cells.

VI. CONCLUSIONS

Key aspects of STM observations of Ru NC formation on Ru(0001)-supported monolayer graphene are described

by fully atomistic modeling. This modeling incorporates reasonable energetic parameters to describe adsorption and diffusion of Ru adatoms accounting for the coarse-scale periodic modulation due to the moiré structure. Specifically, we can describe the increase in the number of NC (i.e. the filling factor) during deposition, as well as that of the NC size and height distributions. Of particular interest is a subtle spatial ordering including a propensity for row formation in the NC array. This is also characterized in detail by considering both the populations of various distinctive local motifs of NCs as well as traditional SRO parameters.

APPENDIX: DFT ANALYSIS FOR Ru ON FREESTANDING GRAPHENE

Our first-principles calculations are performed based on the density functional theory (DFT) with generalized gradient approximation (GGA) in the form of PBE (Perdew–Burke–Ernzerhof)[44] implemented in the Vienna *ab initio* simulation package (VASP)[45–47] code, including spin polarization and dipole moment corrections.[48] Valence electrons are treated explicitly and their interactions with ionic cores are described by PAW[49,50] (projector augmented wave) pseudopotentials.

The wave functions are expanded in a plane-wave basis set with an energy cutoff of 600 eV.

The adatom/freestanding single-layer graphene system is modeled by one adatom in a 4×4 parallelogram graphene supercell and with periodic boundary conditions.[51,52] The primitive cell of graphene is a parallelogram with two carbon atoms. The lattice constant obtained from the first-principles calculation is 2.46 Å, which agrees well with experimental value. The dimension of the supercell in the direction orthogonal to the graphene sheet is 15 Å, which allows a vacuum region of about 12 Å to separate the atoms in the supercell and their replicas. The calculations are performed for adatoms positioned on graphene at the top of a carbon atom, labeled top (T) site, at the middle of a carbon-carbon bond, labeled bridge (B) site, and at the hexagonal center site, labeled hollow (H) site, respectively. A k-point sampling of $6 \times 6 \times 1$ Monkhorst–Pack grids in the first Brillouin zone of the supercell and a Gaussian smearing with a width of $\sigma = 0.05$ eV are used in the calculations. All atoms in the supercell are allowed to relax until the forces on each atom are smaller than 0.01 eV/Å. The supercell dimensions are kept fixed during the relaxation.

The adsorption energy E_{ads} is defined as the difference between the energy of the relaxed adatom/graphene system and that of the isolated perfect graphene sheet and an isolated adatom. To minimize the error in the adsorption energy calculations, the energies of the isolated perfect graphene sheet and an isolated atom are also calculated using the same supercell, plane-wave basis, and k-point sampling as those in the calculations for the adatom/graphene systems. We obtain $E_{ads}(H) = -1.97$ eV, $E_{ads}(T) = -1.35$ eV, and $E_{ads}(B) = -1.21$ eV.

In principle, the diffusion barriers should be obtained by examining the potential energy surfaces for the adatoms on the substrate. However, in the case of adatoms on graphene, the adsorption geometry is relatively simple due to the high symmetry of the graphene lattice. Thus, the diffusion barrier $E_d = 0.62$ eV (in this case corresponding to hopping between H sites over the T site) can be accurately evaluated by examining the energy difference between the different adsorption sites.[51,52]

*Current address: TUM Create Research Center, 62 Nanyang Dr., Singapore 637459.

†Corresponding author: yong@ameslab.gov

[1] M. Batzill, Surf. Sci. Rep. **67**, 83 (2012).

[2] A. B. Preobrajenski, M. L. Ng, A. S. Vinogradov, and M. Martensson, Phys. Rev. B **78**, 073401 (2008).

[3] A. T. N'Diaye, S. Bleikamp, P. J. Feibelman, and T. Michely, Phys. Rev. Lett. **97**, 215501 (2006).

[4] J. Coraux, A. T. N'Diaye, C. Busse, and T. Michely, Nano Lett. **8**, 565 (2008).

[5] J. Coraux, T. N. Plasa, C. Busse, and T. Michely, New J. Phys. **10**, 043033 (2008).

[6] A. T. N'Diaye, T. Gerber, C. Busse, J. Myslivecek, J. Coraux, and T. Michely, New J. Phys. **11**, 103045 (2009).

[7] S. Marchini, S. Günther, and J. Wintterlin, Phys. Rev. B **76**, 075429 (2007).

[8] B. Wang, M.-L. Bocquet, S. Marchini, S. Gunther, and J. Wintterlin, Phys. Chem. Chem. Phys. **10**, 3530 (2008).

[9] A. L. Vázquez de Parga, F. Calleja, B. Borca, M. C. G. Passeggi, J. J. Hinarejos, F. Guinea, and R. Miranda, Phys. Rev. Lett. **100**, 056807 (2008).

[10] B. Wang, M.-L. Bocquet, S. Günther, and J. Wintterlin, Phys. Rev. Lett. **101**, 099703 (2008).

[11] A. L. Vazquez de Parga, F. Calleja, B. Borca, M. C. G. Passeggi, J. J. Hinarejos, F. Guinea, and R. Miranda, Phys. Rev. Lett. **101**, 099704 (2008).

[12] D. Martoccia, P. R. Willmott, T. Brugger, M. Björck, S. Günther, C. M. Schlepütz, A. Cervellino, S. A. Pauli, B. D. Patterson, S. Marchini, J. Wintterlin, W. Moritz, and T. Greber, Phys. Rev. Lett. **101**, 126102 (2008).

[13] P. W. Sutter, J.-I. Flege, and E. A. Sutter, Nat. Mater. **7**, 406 (2008).

[14] Y. Pan, H. Zhang, D. Shi, J. Sun, S. Du, F. Liu, and H.-J. Gao, Adv. Mater. **21**, 2777 (2009).

[15] B. Wang, S. Gunther, J. Wintterlin, and M.-L. Bocquet, New J. Phys. **12**, 043041 (2010).

[16] W. Moritz, B. Wang, M.-L. Bocquet, T. Brugger, T. Greber, J. Wintterlin, and S. Günther, Phys. Rev. Lett. **104**, 136102 (2010).

[17] D. Stradi, S. Barja, C. Díaz, M. Garnica, B. Borca, J. J. Hinarejos, D. Sánchez-Portal, M. Alcamí, A. Arnau, A. L. Vázquez de Parga, R. Miranda, and F. Martín, Phys. Rev. Lett. **106**, 186102 (2011).

[18] M. Gyamfi, T. Eelbo, M. Wasniowska, and R. Wiesendanger, Phys. Rev. B **83**, 153418 (2011).

[19] A. Politano, B. Borca, M. Minniti, J. J. Hinarejos, A. L. Vazquez de Parga, D. Farias, and R. Miranda, Phys. Rev. B **84**, 035450 (2011).

[20] K. Katsiev, Y. Losovyj, Z. Zhou, E. Vevesco, L. Liu, P. A. Dowben, and D. W. Goodman, Phys. Rev. B **85**, 195405 (2012).

[21] B. Borca, S. Barja, M. Garnica, M. Minniti, A. Politano, J. M. Rodriguez-García, J. J. Hinarejos, D. Farías, A. L. Vázquez de Parga, and R. Miranda, New J. Phys. **12**, 093018 (2010).

[22] Y. Pan, M. Gao, L. Huang, F. Liu, and H.-J. Gao, Appl. Phys. Lett. **95**, 093106 (2009).

[23] K. Donner and P. Jakob, J. Chem. Phys. **131**, 164701 (2009).

[24] H. Zhang, Q. Fu, Y. Cui, D. Tan, and X. Bao, Chin. Sci. Bull. **54**, 2446 (2009).

[25] Z. Zhou, F. Gao, and D. W. Goodman, Surf. Sci. **604**, L31 (2010).

[26] E. Sutter, P. Albrecht, B. Wang, M.-L. Bocquet, L. Wu, Y. Zhu, and P. Sutter, Surf. Sci. **605**, 1676 (2011).

[27] Q. Liao, H. J. Zhang, K. Wu, H. Y. Li, S. N. Bao, and P. He, Nanotechnology **22**, 125303 (2011).

[28] Y. Xu, L. Semidey-Flecha, L. Liu, Z. Zhou, and D. W. Goodman, Faraday Discuss. **152**, 267 (2011).

[29] M. Sicot, S. Bouvron, O. Zander, U. Rudiger, Y. S. Dedkov, and M. Fonin, Appl. Phys. Lett. **96**, 093115 (2010).

[30] J. A. Venables, G. D. T. Spiller, and M. Handbucken, Rep. Prog. Phys. **47**, 399 (1984).

[31] J. W. Evans, P. A. Thiel, and M. C. Bartelt, Surf. Sci. Rep. **61**, 1 (2006).

[32] J. G. Kirkwood, J. Chem. Phys. **3**, 300 (1935).

[33] R. K. Pathria, *Statistical Mechanics* (Permagon, Oxford, 1972).

[34] M. C. Bartelt and J. W. Evans, Phys. Rev. B **46**, 12675 (1992).

[35] M. C. Bartelt, M. C. Tringides, and J. W. Evans, Phys. Rev. B **47**, 13891 (1993).

[36] M. C. Bartelt and J. W. Evans, Surf. Sci. Lett. **284**, L437 (1993).

[37] Only values of E_{ads} determined from this form at discrete triangular lattice of adsorption sites provide input to the model.

[38] X. Niu, R. Vardavas, R. E. Caflisch, and C. Ratsch, Phys. Rev. B **74**, 193403 (2006).

[39] O. V. Yazyev and A. Pasquarello, Phys. Rev. B **82**, 045407 (2010).

[40] A. Ishii, M. Yamamoto, H. Asano, and K. Fujiwara, J. Phys.: Conf. Ser. **100**, 052087 (2008).

[41] N. Nakada and A. Ishii, Solid State Commun. **151**, 13 (2011).

[42] Some moiré cells can contain only isolated Ru adatoms when deposition ends. These might aggregate with existing NCs in nearby cells or nucleate new NCs (Ref. 3). We find that such postdeposition effects are negligible except for very low coverages.

[43] The smallest stable NC for $h = 2$ has five atoms in the first layer supporting two in the second. For $h = 3$, 10 in the first layer support five in the second supporting two in the third, etc.

[44] J. P. Perdew, K. Burke, and M. Ernzerhof, Phys. Rev. Lett. **77**, 3865 (1996).

[45] G. Kresse and J. Furthmüller, Comput. Mater. Sci. **6**, 15 (1996).

[46] G. Kresse and J. Hafner, Phys. Rev. B **47**, 558 (1993).

[47] G. Kresse and J. Furthmüller, Phys. Rev. B **54**, 11169 (1996).

[48] G. Makov and M. C. Payne, Phys. Rev. B **51**, 4014 (1995).

[49] P. E. Blöchl, Phys. Rev. B **50**, 17953 (1994).

[50] G. Kresse and D. Joubert, Phys. Rev. B **59**, 1758 (1999).

[51] X. Liu, C. Z. Wang, Y. X. Yao, W. C. Lu, M. Hupalo, M. C. Tringides, and K. M. Ho, Phys. Rev. B **83**, 235411 (2011).

[52] M. Hupalo, X. Liu, C. Z. Wang, W. C. Lu, Y. X. Yao, K. M. Ho, and M. C. Tringides, Adv. Mater. **23**, 2082 (2011).